High-Sensitivity Fiber Bragg Grating Pressure Sensor With a Hinged-Lever Structure

Qiang Liu, Shuhui Wei, Shenglong Gu, Jian Han, Chao Ma, Pengfei Lu, Jingwei Lv, Paul K. Chu, *Fellow, IEEE*, and Chao Liu

***Abstract*—This article presents a high-sensitivity fiber Bragg grating (FBG) pressure sensor with a metal diaphragm and hinge-lever structure designed for small-range pressure measurement. The sensor employs hinge groups and dual-lever structure to amplify the small strain induced by diaphragm deformation, thereby enhancing sensitivity. The sensor structure is analyzed and optimized by the finite element method. The sensor is fabricated and tested on a pressure calibration platform. The experimental data show that the pressure sensitivity of the sensor is 3.382 pm/kPa in the range of 0–1 MPa, and the correlation coefficient is 0.9999. Another FBG is employed to compensate for the influence of temperature with a sensitivity of 12.14 pm/°C in the range of 20 °C–70 °C and the correlation coefficient of 0.9998. In addition, the sensor is capable of maintaining stable pressure measurements within the temperature range of 25 °C–55 °C. The sensor with high sensitivity and stability is suitable for low-pressure, high-sensitivity detection.**

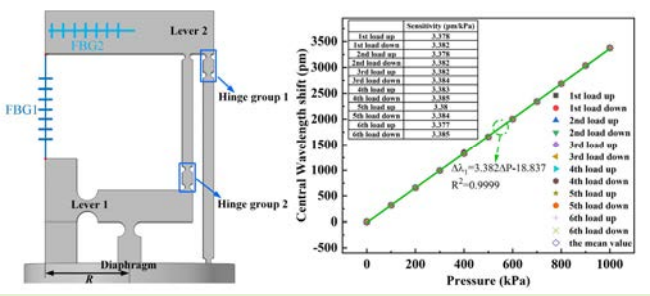

***Index Terms*— Fiber Bragg grating (FBG), hinge-lever structure, pressure sensor, temperature sensor.**

Received 15 April 2025; accepted 23 June 2025. Date of publication 2 July 2025; date of current version 1 August 2025. This work was supported in part by the Basic Research Support Project for the Excellent Youth Scholars of Heilongjiang Province under Grant YQJH2023077, in part by Hainan Province Science and Technology Special Fund under Grant ZDYF2022GXJS222, in part by the National Natural Science Foundation of China under Grant 12304480, in part by Heilongjiang Provincial Natural Science Foundation of China under Grant JQ2023F001, in part by the Local Universities Reformation and Development Personnel Training Supporting Project from Central Authorities, in part by the Natural Science Foundation of Heilongjiang Province under Grant LH2021F007, in part by China Postdoctoral Science Foundation under Grant 2020M670881, and in part by the City University of Hong Kong Donation Research Grants under Grant DON-RMG 9229021 and Grant 9220061. The associate editor coordinating the review of this article and approving it for publication was Prof. Agostino Iadicicco. *(Corresponding author: Chao Liu.)*

Qiang Liu, Shuhui Wei, Jian Han, Chao Ma, Pengfei Lu, Jingwei Lv, and Chao Liu are with the Sanya Offshore Oil and Gas Research Institute, Northeast Petroleum University, Sanya 572024, China, and also with the School of Physics and Electronic Engineering, Northeast Petroleum University, Daqing 163318, China (e-mail: nepulq@126.com; wsh010131@163.com; han-jian@126.com; 18003620078@163.com; 327138829@qq.com; lvjingwei2009123@126.com; msm-liu@126.com).

Shenglong Gu is with Logging and Testing Services Company, Daqing Oilfield Company Ltd., Daqing 163100, China (e-mail: 14050460@qq.com).

Paul K. Chu is with the Department of Physics, the Department of Materials Science and Engineering, and the Department of Biomedical Engineering, City University of Hong Kong, Hong Kong, China (e-mail: paul.chu@cityu.edu.hk).

Digital Object Identifier 10.1109/JSEN.2025.3583300

I. Introduction

PRESSURE measurement is important in industrial production. The traditional pressure measurement predominantly relies on electronic sensors that can be influenced by the specific environments resulting in unstable signals [1]. In this respect, the fiber Bragg grating (FBG) sensors have attracted significant attention due to anti-electromagnetic interference, corrosion resistance, stable signal transmission, and quasi-distributed measurements [2]. FBG-based pressure sensors utilize the strain sensitivity of the FBG. The conventional FBG pressure sensor is typically attached to the sensing structures, such as elastic diaphragms [3], [4], [5], [6], thin-walled cylinders [7], [8], [9], metal bellow [10], [11], spring structure [2], and lever structure [12]. However, these direct strain-measuring structures often exhibit relatively low sensitivity. In order to improve the sensitivity, researchers have explored integrating sensitivity and enhanced structures on the diaphragms.

The size and thickness of the elastic metal diaphragm and the sensitivity-enhancing structure determine the measurement range and sensitivity of the sensor. Therefore, the diaphragm-based FBG pressure sensors can have a large measurement range and a small measurement range. With regard to diaphragm-based FBG pressure sensors with a large measurement range, Xu et al. [1] have proposed a

single-lever structure with a diaphragm with an effective radius of 4 mm and thickness of 2 mm. The pressure and temperature can be measured simultaneously, with sensitivities of 29.76 pm/MPa in the range of 0–30 MPa and 32.66 pm/°C in the range of 50 °C–200 °C, respectively. Feng et al. [13] have reported a temperature-pressure sensor with a specially shaped bracket structure. The thickness and effective radius of the diaphragm are 2.5 and 5 mm, respectively. The sensor exhibits a temperature sensitivity of 31.8 pm/°C in the range of 50 °C–200 °C and pressure sensitivity of 50.6 pm/MPa in the range of 0–40 MPa. To achieve a small measurement range and produce a high-sensitivity pressure sensor, Liu et al. [14] have proposed an FBG pressure sensor based on a dual-lever structure with a metal diaphragm. The diaphragm, with a thickness of 0.8 mm and an effective radius of 10 mm, shows a pressure sensitivity of 5.227 pm/kPa in the range of 0–1 MPa. Zhu et al. [4] have proposed a temperature and pressure sensor with a large metal diaphragm of 32 mm effective radius and 1.2 mm thickness. The sensor delivers reliable performance in the temperature range of 30 °C–80 °C and pressure range of 0–1 MPa, with temperature and pressure sensitivities of 12.05 pm/°C and 3.643 pm/kPa, respectively. Zhang et al. [15] have reported a pressure sensor for static ice pressure monitoring with a larger diaphragm radius. The diaphragm with a 55 mm effective radius and 1.2 mm thickness has a pressure sensitivity of 1.89 pm/kPa in the range of 100–500 kPa. Li et al. [16] have proposed a high-precision pressure sensor for low-pressure environments, utilizing a diaphragm of 6 mm effective radius and 0.2 mm thickness. The sensor has a pressure sensitivity of 4.31 pm/kPa in the 0–200-kPa range.

These previous studies reveal that high-sensitivity pressure sensors typically require a thinner metal diaphragm and a larger effective radius. However, an excessively thin and large diaphragm restricts the pressure measurement range and increases the sensor size. In this article, a compact FBG sensor for simultaneous temperature and pressure measurement is designed and investigated, integrating a metal diaphragm with a hinge-lever structure. A novel design approach utilizing hinge groups is proposed to enhance the elastic deformation of the lever structure, thereby improving the sensor's sensitivity. Furthermore, this multihinge configuration ensures uniform strain distribution across the sensor, mitigates stress concentration, and enhances mechanical stability. The sensor achieves a pressure sensitivity of 3.382 pm/kPa in the range of 0–1 MPa. Another FBG is employed to eliminate the influence of temperature. The temperature sensitivity is 12.14 pm/°C in the range of 20 °C–70 °C. The sensor can perform stable pressure measurements in low-pressure ranges.

II. Design and Sensing Principle

A. Principle of FBG

An FBG is an optical fiber device, in which the refractive index of the core is periodically modulated. When the light wave from a broadband source propagates through the fiber grating, the light waves satisfying the Bragg condition are reflected to produce a reflection spectrum. The Bragg wavelength λ_B can be expressed as [17], [18]

$$\lambda_B = 2n_{\text{eff}}\Lambda \tag{1}$$

where n_{eff} and Λ are the effective refractive index and grating period of the FBG, respectively. When the external environmental parameters, such as strain and temperature, change, these two physical parameters are changed, resulting in a shift of the Bragg wavelength. The effects of strain and temperature on the Bragg wavelength shift can be expressed as [19], [20]

$$\frac{\Delta\lambda_B}{\lambda_B} = (1 - P_e)\varepsilon + \left(\xi_f + \alpha_f\right)\Delta T \tag{2}$$

where $\Delta\lambda_B$ represents the shift of the Bragg wavelength, ε is the strain of FBG, ΔT is the temperature variation, P_e is the elastic-optical coefficient, ξ_f is the thermo-optical coefficient, and α_f is the thermal expansion coefficient. According to the above equation, the strain and temperature can be measured based on the Bragg wavelength shift of FBG.

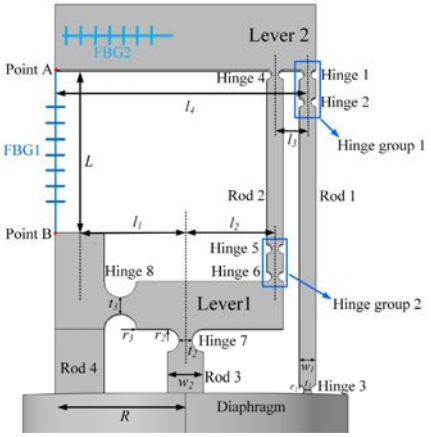

Fig. 1. Planar view of the hinge-lever structure.

B. Sensor Design

The metal diaphragm and hinge-lever structure are shown in Fig. 1. The base is a metal diaphragm with an effective radius R and thickness H, while the upper section incorporates a sensitivity-enhancing structure with thickness b, including two levers and eight circular hinges. A smaller effective radius R of the diaphragm can effectively control the size of the sensor, the thicker b of the sensitization structure improves the stability and reliability of the sensor, and the multihinge structure reduces stress concentration, thereby enhances the service life. Specifically, Hinges 1 and 2 constitute Hinge group 1, and Hinges 5 and 6 constitute Hinge group 2. FBG1 and FBG2 are utilized to measure the pressure and temperature, respectively. The detailed parameters of the structure are summarized in Table I.

The force analysis of the hinge-lever structure is illustrated in Fig. 2. When pressure is applied to the bottom of the diaphragm, the maximum stress concentrates on its center, causing Rod 3 and the hinge-lever structure to deform. Due to the stiffness of the hinge-lever metal structure, it imposes a resistance to the diaphragm deformation, resulting in

TABLE I
PARAMETERS OF THE SENSOR

Symbol	Description (units)	Value
R	Effective radius of diaphragm (mm)	8.0
H	Thickness of diaphragm (mm)	0.7
w_1	Width of the Rod 1 (mm)	1.0
w_2	Width of the Rod 3 (mm)	2.2
b	Thickness of hinge-lever Structure (mm)	2.0
l_1	Length of Rod 3 to Rod 4 (mm)	6.5
l_2	Length of Rod 2 to Rod 3 (mm)	5.5
l_3	Length of Rod 1 to Rod 2 (mm)	2.0
l_4	Length of Rod 1 to Point A (mm)	15.5
r_1	Radius of Hinges 1-6 (mm)	0.3
r_2	Radius of Hinge 7 (mm)	0.7
r_3	Radius of Hinge 8 (mm)	1.0
t_1	Waist width of Hinges 1-6 (mm)	0.4
t_2	Waist width of Hinge 7 (mm)	0.8
t_3	Waist width of Hinge 8 (mm)	1.0
E_f	Young's modulus of optical fiber (GPa)	70
E	Young's modulus of structure (GPa)	200
μ_f	Poisson's ratio of optical fiber	0.22
A_f	Cross-sectional area of the optical fiber (m^2)	1.22×10^{-8}
μ	Poisson's ratio of structure	0.3
ρ	The density of structure (kg/m^3)	8000

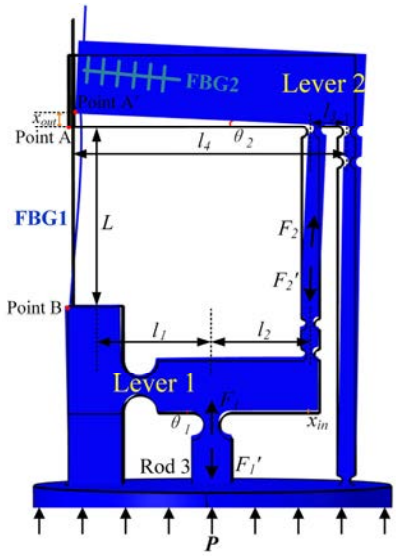

Fig. 2. Force analysis of the hinge-lever structure.

interaction forces F_1 and F_1' between the diaphragm and the hinge-lever structure. Under the influence of F_1, Lever 1 rotates counterclockwise around its left pivoted by an angle θ_1. According to the lever principle, a downward force F_2' is generated at the right end of Hinge 1, and the opposite F_2 is equal to F_2'. Under the influence of F_2, Lever 2 rotates clockwise around its right pivot by θ_2. Therefore, Point A moves to Point A′. This process converts the diaphragm pressure to axial strain of FBG1.

The point A displacement of the hinge-lever structure is relatively small and can be approximated as x_{out}. x_{out} and the strain of FBG1 are, respectively, expressed as

$$x_{\text{out}} = F_1/k_a \tag{3}$$
$$\varepsilon = x_{\text{out}}/L \tag{4}$$

where k_a is the stiffness of the hinge-lever structure, and L is the distance between Points A and B. According to the principle of leverage, the equilibrium equations for Levers 1 and 2 can be derived as follows:

$$F_1 l_1 = F_2'(l_1 + l_2) + K_{M2}\theta_1 + K_{M3}\theta_1 \tag{5}$$
$$F_2 l_3 = K_{M1}\theta_2 + k_f x_{\text{out}} l_4 \tag{6}$$

where l_1 and $l_1 + l_2$ represent the lengths from the input and output terminals of Lever 1 to the pivot, respectively, l_3 and l_4 are the lengths from the input and output terminals of Lever 2 to the pivot, K_{M1}, K_{M2}, and K_{M3} denote the rotational stiffnesses of Hinges 1–6, 7, and 8, respectively, and k_f is the elastic modulus of the optical fiber, which can be treated as a spring. The values of k_f, θ_1, and θ_2 are approximately expressed as

$$k_f = \frac{A_f E_f}{L} \tag{7}$$
$$\theta_1 = \frac{x_{\text{in}}}{l_1 + l_2} \tag{8}$$
$$\theta_2 = \frac{x_{\text{out}}}{l_4}. \tag{9}$$

As shown in Fig. 1, for $s_1 = r_1/t_1$, the rotational stiffness K_{M1} of Hinges 1–6 is expressed in (10) [21], while the stiffnesses K_{M2} and K_{M3} of Hinges 7 and 8 are derived similarly and are not repeated here

$$K_{M1} = \frac{Ebr_1^2}{12}\left[\frac{2s_1^3(6s_1^2+4s_1+1)}{(2s_1+1)(4s_1+1)^2} + \frac{12s_1^4(2s_1+1)}{(4s_1+1)^{5/2}}\arctan\sqrt{4s_1+1}\right]^{-1}. \tag{10}$$

Combining (3)–(10), the stiffness of the hinge-lever structure can be obtained as follows:

$$k_a = \frac{(k_{M1}x_{\text{out}} + k_f x_{\text{out}} l_4^2)(l_1+l_2)^2 + x_{\text{in}} l_3 l_4 (K_{M2}+K_{M3})}{(l_1+l_2) l_1 l_3 l_4 x_{\text{out}}}. \tag{11}$$

According to the elasticity theory, as an external pressure acts on a diaphragm, the pressure P applied to the diaphragm and the supporting force F_1' from the hinge-lever structure produce two deflections at the diaphragm center [22]

$$\omega_1 = \frac{3(1-\mu)^2 P R^4}{16 E H^3}\left[1 - \left(\frac{w_2}{2R}\right)^4 + 4\left(\frac{w_2}{2R}\right)^2 \ln\frac{w_2}{2R}\right] \tag{12}$$
$$\omega_2 = \frac{3(1-\mu)^2 F_1 R^4}{4\pi E H^3}\left[1 - \left(\frac{w_2}{2R}\right)^2 \cdot \left(1 + \frac{4\ln^2\left(\frac{w_2}{2R}\right)}{1-\left(\frac{w_2}{2R}\right)^2}\right)\right]. \tag{13}$$

Thus, the actual maximum deflection of the diaphragm can be expressed as

$$\omega_{\max} = \omega_1 - \omega_2. \tag{14}$$

The metal diaphragm is integrated with the hinge-lever structure through Rod 3. The relationship between the maximum deflection of the diaphragm and the output

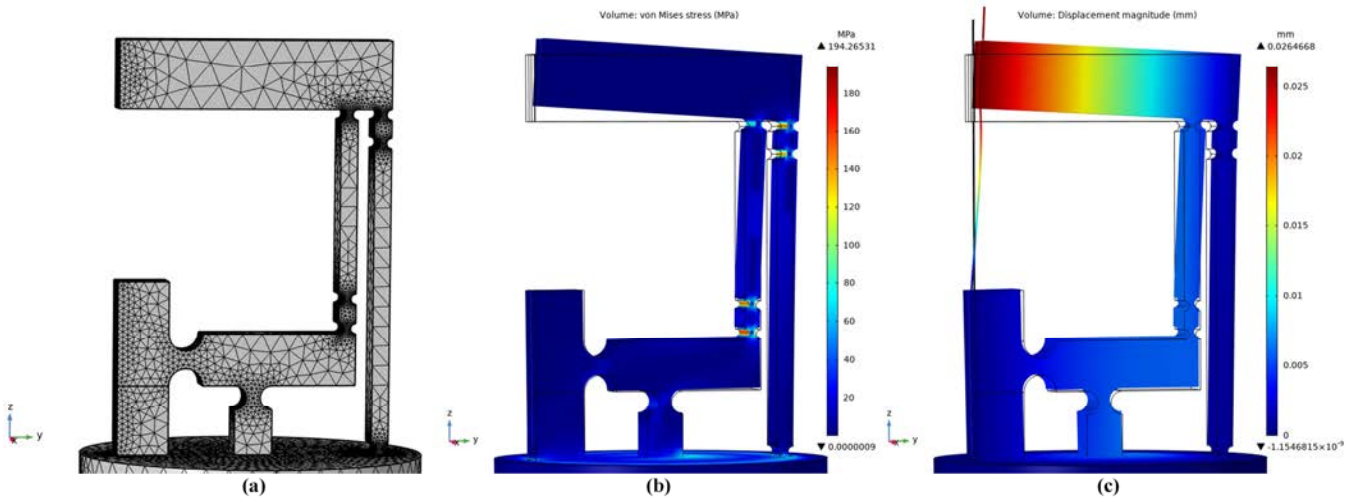

Fig. 3. Simulation of the sensor. (a) Mesh division. (b) Stress distribution. (c) Displacement distribution.

displacement of the hinge-lever structure can be computed as follows:

$$x_{\text{out}} = \kappa \omega_{\max} \tag{15}$$

where κ is the displacement amplification factor of the hinge-lever structure [23]. Combining (3) and (11)–(15)

$$\kappa = \frac{F_1}{k_a(\omega_1 - \omega_2)}. \tag{16}$$

Substituting (12)–(16) into (2) and setting $\Delta T = 0$, the wavelength shift of FBG1 can be obtained as

$$\frac{\Delta\lambda_1}{\lambda_1} = \frac{F_1(1-P_e)L(l_1+l_2)l_1l_3l_4x_{\text{out}}}{\left[\left(k_{M1}x_{\text{out}} + k_f x_{\text{out}} l_4^2\right)(l_1+l_2)^2 + x_{\text{in}} l_3 l_4 (K_{M2}+K_{M3})\right]}. \tag{17}$$

III. Finite Element Analysis and Optimization

To ensure that the sensor can operate within the 0–1-MPa range, the structure must remain below the yield strength under maximum stress, meaning that the deformation is elastic and recoverable. The finite element software COMSOL [24] is used to construct the structure and analyze the mechanical characteristic. The sensor is made of 304 stainless steel (Young's modulus $E = 200$ GPa, Poisson's ratio $\mu = 0.3$, density $\rho = 8000$ kg/m^3, and thermal expansion coefficient 17×10^{-6}/°C). The simulation model of the hinge-lever structure, which uses ultrafine mesh division, is shown in Fig. 3(a). The fixed constraint is applied to the boundary of the metal diaphragm, while the load is applied to the metal diaphragm with the effective radius of diaphragm. As the bottom diaphragm of the sensing structure is subjected to a pressure of 1 MPa, the stress distribution is shown in Fig. 3(b). The maximum displacement occurs at Point A. The maximum stress position appears at Hinge groups 1 and 2. The maximum values are 158.25 and 194.27 MPa, respectively, which are less than the yield strength of 205 MPa of 304 stainless steel [25]. The FBG1 (Young's modulus $E_f = 70$ GPa, Poisson's ratio $\mu_f = 0.22$, and density $\rho_f = 2200$ kg/m^3) is bonded between Points A and B of the hinge-lever structure to analyze the wavelength-pressure sensitivity. For a pressure of 1 MPa, the displacement in the z-direction is shown in Fig. 3(c). The displacement is amplified by the two lever structures, and it is transferred to the axial strain of the FBG1. The relationship between the wavelength shift of FBG1 and the applied pressure can be used to optimize the sensor and evaluate its performance.

The structure is optimized based on the initial structural parameters provided in Table I. The impact of the diaphragm thickness is shown in Fig. 4(a). As the pressure is 1 MPa, the sensitivity and maximum stress of the sensor decrease with increasing diaphragm thickness. It is because a larger thickness enhances the diaphragm stiffness and restricts deformation. In order to ensure that the maximum stress is lower than the yield strength of 205 MPa, the diaphragm thickness is set to 0.7 mm. Fig. 4(b) shows the effect of Rod 1 on the sensor. The sensitivity and maximum stress of the hinge decrease with increasing Rod 1 width. Because a wider Rod 1 has greater stiffness, it restricts elastic deformation and reduces the displacement of point A. Consequently, the width of Rod 1 is set to 1 mm. Fig. 4(c) shows the effect of the radius of Hinges 1–6. A larger radius improves the sensitivity and raises the maximum stress, but the larger radius results in narrower hinges. Considering the manufacturing feasibility, $r_1 = 0.3$ mm is chosen as the radius of Hinges 1–6. Fig. 4(d) describes the effects of the Rod 3 width. As the width of Rod 3 increases, the sensitivity initially increases and then gradually decreases. It is because the strain of the diaphragm is not uniform, and the center of the diaphragm experiences the maximum strain. A narrower Rod 3 has a smaller contact area with the diaphragm, enabling it to capture the maximum strain. However, a narrower Rod 3 has smaller stiffness. Hence, Rod 3 is prone to deformation, thus reducing its ability to transform strain from the diaphragm. The increase in Rod 3 width results in bigger contact area with the diaphragm. It decreases the strain transformed from the diaphragm and the stiffness

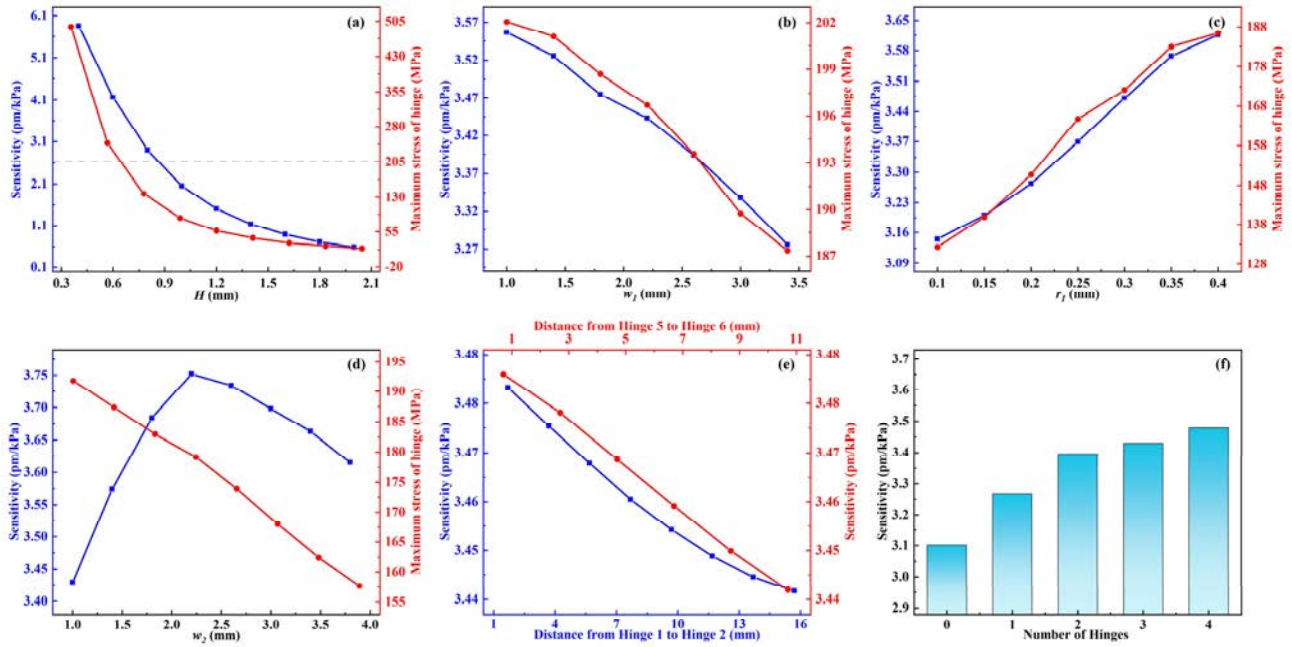

Fig. 4. Effect of the structural parameters on sensitivity and maximum hinge stress. (a) Diaphragm thickness. (b) Width of Rod 1. (c) Radius of Hinges 1–6. (d) Width of Rod 3. (e) Distances from Hinge 1 to Hinge 2 and from Hinge 5 to Hinge 6. (f) Number of hinges.

increases. Therefore, there exists an optimal sensitivity, and the width of Rod 3 is set to 2.2 mm.

Fig. 4(e) shows the effect of the distances from Hinge 1 to 2. As Hinge 1 is fixed, a smaller distance increases the sensitivity. This is because a smaller distance enhances the elastic deformation of Hinge group 1 to improve the sensitivity. Similarly, the distance between Hinges 5 and 6 has a comparable effect on the sensitivity. Considering the manufacturing constrain, the distance between Hinges 1 and 2 and between Hinges 5 and 6 is set to 1.7 mm. Fig. 4(f) compares the effect of the hinge number on the sensitivity. Bar 0 shows that the sensor only has Hinges 3, 4, 7, and 8. Bars 1–4 show that Hinges 1, 6, 2, and 5 are added sequentially. It is clear that Hinges 2 and 5 significantly improve the sensitivity. Hence, the two hinge groups can enhance the elastic deformation of the structure and improve the sensitivity of the sensor.

After the hinge-lever structure was optimized, the simulated wavelength sensitivity of FBG1 can be calculated by the following steps.

1) The displacement ΔL of Points A and B can be obtained from the simulation result for different pressures, and the displacement ΔL is linearly increase with the pressure. The initial distance L between A and B is 10 mm, and the strain can be calculated by $\Delta L/L$.
2) The strain sensitivity of FBG1 has been measured in the experiment, and the value is $S_{\text{strain}} = 1.34$ pm/$\mu\varepsilon$.
3) The wavelength shift of FBG1 is calculated by $S_{\text{strain}} \times (\Delta L/L) \times 10^6/1000$; then, the wavelength sensitivity is obtained. As the pressure is 1 MPa, ΔL is 0.02596 mm. It means that the simulated pressure sensitivity is 3.478 pm/kPa, as shown in Fig. 4(f).

IV. Experimental Results

The sensor is fabricated by 304 stainless steel, which has high elasticity modulus, excellent resistance to high temperature, corrosion, and durability in normal environments. The manufacturing tolerance is ± 0.1 mm. The sensing structure includes hollow circular tube with external thread and the upper hinge-lever structure. The upper hinge lever is welded onto the surface of the hollow circular tube. As the top metal diaphragm of the hollow circular tube senses the pressure, the strain is transferred to Rod 3 of the hinge-lever structure. The fabricated sensor has a compact design with an outer diameter of 28 mm and a height of 60 mm. Two (FBG1 and FBG2), with Bragg wavelengths of 1555 and 1550 nm, are bonded using 353ND epoxy adhesive at the region of Points A and B and the surface of Lever 2. The thermal expansion coefficient of 353ND epoxy adhesive is 60×10^{-6}/°C, which is similar with 304 stainless steel. During the bonding process, the pretension is applied to the FBGs using precision displacement platform; then, FBG is bonded with 100 microstrain. After the bonding, the sensor is heated in an oven to 120 °C for 10 min to cure the 353ND epoxy adhesive.

The pressure testing system is assembled using a standard pressure gauge (measuring range: 0–1.6 MPa and accuracy level: 0.25), pressure calibration instrument, computer, and FBG demodulator (MOI SM125, accuracy: 1 pm), as shown in Fig. 5. The relationship between the pressure and Bragg wavelengths is established by applying hydraulic pressure.

The temperature testing system utilizes far-infrared fast-drying oven to measure the temperature characteristics of FBG1 and FBG2, as shown in Fig. 6.

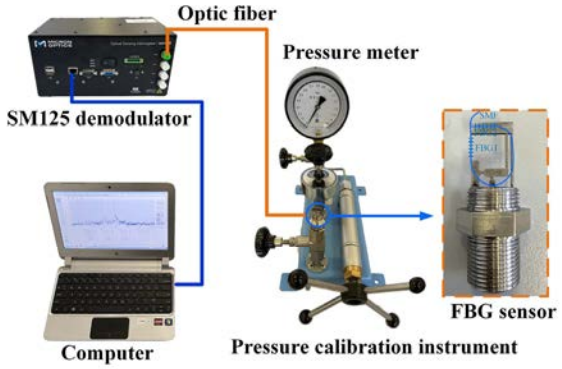

Fig. 5. Pressure testing system.

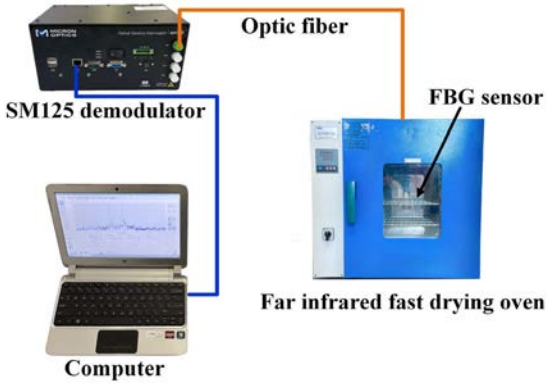

Fig. 6. Temperature testing system.

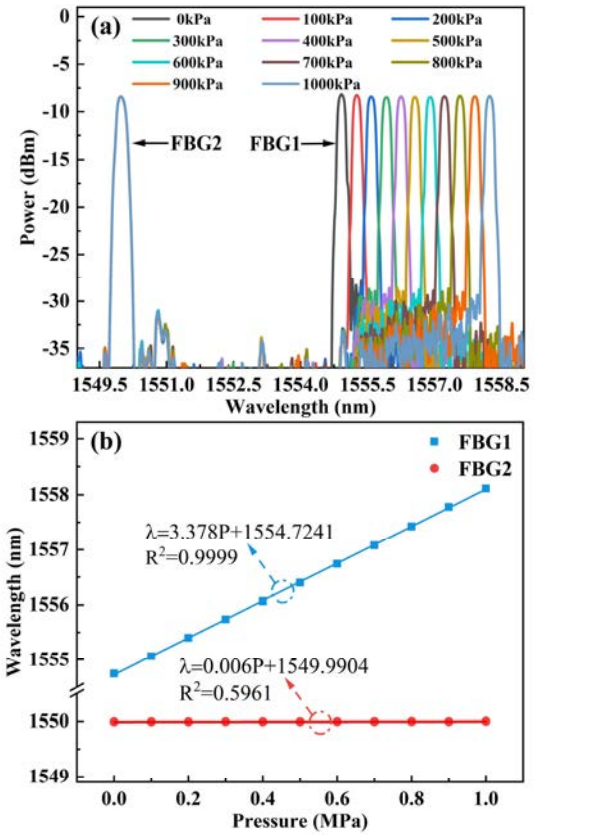

Fig. 7. Reflection spectrum and sensitivity of the pressure experiment. (a) Reflection spectra. (b) Variation of the center wavelength with pressure.

The sensing characteristics of the pressure sensor are determined at room temperature (25 °C). As the pressure is increased from 0 to 1 MPa, the reflection spectra of FBG1 and FBG2 are obtained and presented in Fig. 7(a). The reflection spectra of FBG1 shift to a longer wavelength, while the reflection spectra of FBG2 remain unchanged. The center wavelengths of FBG1 and FBG2 are plotted in Fig. 7(b). The center wavelengths of FBG1 increase linearly with pressure with a fitted slope of 3.378 pm/kPa. The center wavelength of FBG2 is nearly unchanged, and the slope of 0.0006 pm/kPa can be perceived as an error. Hence, the center wavelength of FBG1 exhibits a linear relationship with pressure, while FBG2 is less affected by pressure and can be used as temperature compensation. The sensor can overcome the cross-sensitivity between temperature and pressure. The experimental and simulation results show good consistency, and the small error can be attributed to the errors in mechanical processing and adhesive.

To evaluate the repeatability of the pressure sensor, six consecutive loading–unloading cycles are implemented. Fig. 8(a) shows the center wavelength variation of FBG1 with changing pressure. The fitted slopes show that the sensor has excellent repeatability. The average sensitivity is 3.382 pm/kPa, and the maximum deviation is only 0.147%. The stability of the sensor is evaluated by holding each pressure for 20 s. The experiment is repeated twice with loading–unloading cycles. As shown by the experimental results in Fig. 8(b), the sensor exhibits outstanding stability and rapid response.

In order to evaluate the long-term performance, the sensor is tested for 2 h applied different pressures, as shown in Fig. 9. It can be seen that the peak wavelengths of the two FBGs remain relatively stable for each pressure condition, without significant fluctuations. As the pressure varies, FBG1 responds rapidly; it means that the sensor exhibits excellent long-term stability and pressure resistance.

The temperature characteristics of the sensor are determined in an oven. The sensor is placed in the oven and heated from 20 °C to 70 °C and then cooled to 20 °C. As shown in Fig. 10, FBG1 and FBG2 exhibit similar temperature trends. By means of linear fitting, the average temperature sensitivities of FBG1 and FBG2 are 12.78 and 12.14 pm/°C with linearity $R^2 = 0.9995$ and $R^2 = 0.9998$, demonstrating the feasibility for temperature compensation.

In order to evaluate the pressure-sensing performance at different temperatures, the sensor is heated by heating tape and alumina thermal insulation cotton. It is found that the pressure sensitivity of the designed sensor degrades as the temperature is higher than 55 °C due to softening of the used 353ND epoxy adhesive. The pressure characteristics of the sensor are determined at 35 °C, 45 °C, and 55 °C. As shown in Fig. 11(a), the Bragg wavelengths of FBG1 change linearly with increasing pressure with excellent consistency, while FBG2 does not change with pressure. Fig. 11(b) shows

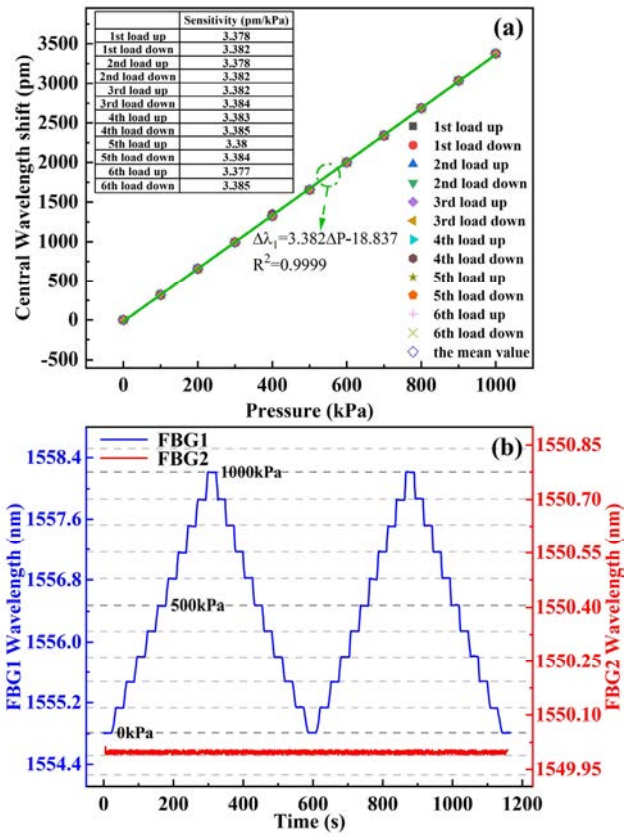

Fig. 8. Repeatability and stability. (a) Center wavelength shifts of FBG1 versus pressure. (b) Variation of the center wavelength versus time.

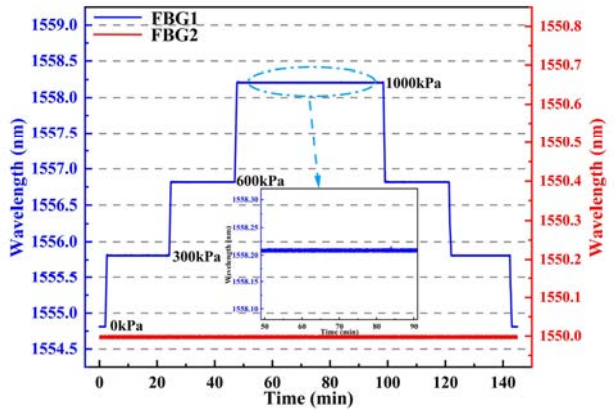

Fig. 9. Response of the sensor for long-term testing.

the relationship between the wavelength shift of FBG1 and pressure at different temperatures. The linearly fitted slopes are close to the pressure sensitivity of 3.382 pm/kPa at room temperature (25 °C), indicating that the sensor remains stable pressure measurement in the temperature range of 25 °C–55 °C.

When employing two FBGs for temperature compensation, a matrix approach can be used to decouple the effects of pressure and temperature, thereby improving measurement accuracy [11]

$$\begin{bmatrix} \Delta\lambda_1 \\ \Delta\lambda_2 \end{bmatrix} = \begin{bmatrix} S_{P1} & S_{T1} \\ S_{P2} & S_{T2} \end{bmatrix} \begin{bmatrix} \Delta P \\ \Delta T \end{bmatrix} \tag{18}$$

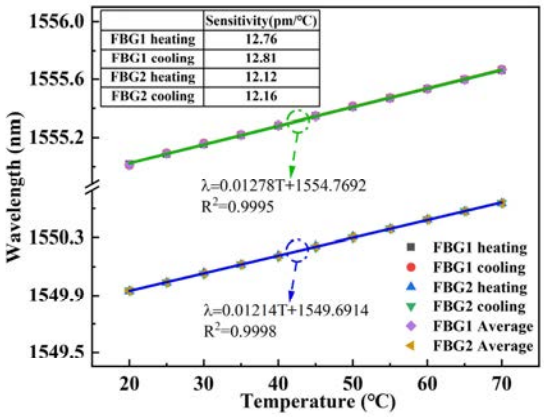

	Sensitivity(pm/°C)
FBG1 heating	12.76
FBG1 cooling	12.81
FBG2 heating	12.12
FBG2 cooling	12.16

Fig. 10. Variation of the center wavelength versus temperature.

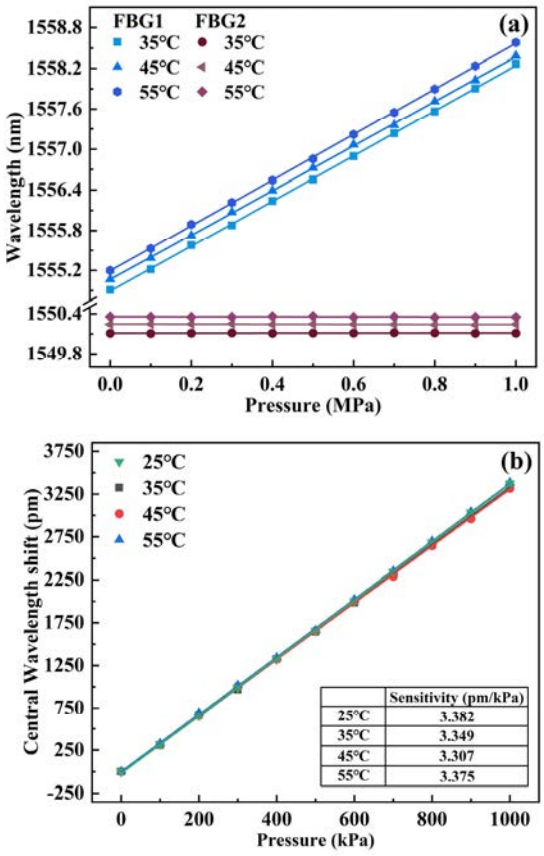

	Sensitivity (pm/kPa)
25°C	3.382
35°C	3.349
45°C	3.307
55°C	3.375

Fig. 11. Sensor assessment at different temperatures. (a) Variation of the center wavelength with pressure at different temperatures. (b) Variation of the center wavelength shift of FBG1 with pressure at different temperatures.

where S_{T1} and S_{T2} are the temperature sensitivities of FBG1 and FBG2, S_{P1} and S_{P2} are the pressure sensitivities of FBG1 and FBG2, and $\Delta\lambda_1$ and $\Delta\lambda_2$ are the Bragg wavelength shifts of FBG1 and FBG2. The pressure change ΔP and temperature change ΔT can be obtained by inverting the matrix

$$\begin{bmatrix} \Delta P \\ \Delta T \end{bmatrix} = \frac{1}{S_{P1}S_{T2} - S_{P2}S_{T1}} \begin{bmatrix} S_{T2} & -S_{T1} \\ -S_{P2} & S_{P1} \end{bmatrix} \begin{bmatrix} \Delta\lambda_1 \\ \Delta\lambda_2 \end{bmatrix}. \tag{19}$$

TABLE II
COMPARISON OF FBG TEMPERATURE AND PRESSURE SENSORS

Ref.	Diaphragm Radius (mm)	Pressure Range (MPa)	Pressure Sensitivity (pm/kPa)	Linearity	Temperature Range (°C)	Temperature Sensitivity (pm/°C)
Venkata[26]	15	0-0.5	16.22	0.9934	-	-
Liu[14]	10	0-1	5.227	0.9999	20-80	12.09
Zhu[4]	32	0-1	3.643	0.9854	30-80	12.055
Zhang[15]	55	0.1-0.5	1.89	0.9915	-	-
Li[16]	6	0-0.2	4.31	0.9995	-	-
Vorathin[27]	NA	0-0.02	77.7	0.9994	29.5-54.5	69.4
This paper	8	0-1	3.382	0.9999	20-55	12.14

By substituting the obtained parameters of S_{T1}, S_{T2}, S_{P1}, and S_{P2}, ΔP and ΔT can be determined

$$\begin{bmatrix} \Delta P \\ \Delta T \end{bmatrix} = \frac{1}{41.05} \begin{bmatrix} 12.14 & -12.78 \\ -0.0006 & 3.382 \end{bmatrix} \begin{bmatrix} \Delta\lambda_1 \\ \Delta\lambda_2 \end{bmatrix}. \quad (20)$$

Table II compares the characteristics of FBG pressure sensors designed for low-pressure ranges reported in recent years. Compared with [4], [14], [15], and [26], the proposed sensor has smaller diaphragm radius; it means that smaller size sensor can be achieved with higher sensitivity and without buckling or nonlinearity. Although the sensor of [16] has smaller diaphragm radius and higher sensitivity, the measurement range of the pressure is narrower. The sensor of [14] has the similar sensing structure and comprehensive performance with our sensor, but our FBG sensor has a smaller effective radius of the diaphragm and better sensitization structure. Meanwhile, the welding is used to assemble the mental diaphragm and hinge-lever structure; the method provides greater reliability and stability for long-term work.

V. CONCLUSION

An FBG pressure sensor comprising a metal diaphragm and hinge-lever structure is designed and optimized. The pressure sensitivity is significantly enhanced by the hinge groups of the double-lever structure. In the pressure range of 0–1 MPa, a pressure sensitivity of 3.382 pm/kPa is achieved. Another FBG (FBG2) with a temperature sensitivity of 12.14 pm/°C is employed for temperature compensation and to eliminate the cross-sensitivity between temperature and pressure. The novel sensor with high sensitivity, compact size, excellent linearity, and repeatability can be operated stably in the temperature range of 25 °C–55 °C, and the sensing structure can be further improved to expand its application field.

REFERENCES

[1] D. Xu, D. Feng, Q. Chen, D. Huo, and X. Qiao, "Compact-packaged and diaphragm-lever structured fiber-optic temperature and pressure sensors for oil and gas well applications," *IEEE Sensors J.*, vol. 22, no. 23, pp. 22670–22677, Dec. 2022, doi: 10.1109/JSEN.2022.3215970.

[2] X. Li et al., "An FBG pressure sensor based on spring-diaphragm elastic structure for ultimate pressure detection," *IEEE Sensors J.*, vol. 22, no. 3, pp. 2213–2220, Feb. 2022, doi: 10.1109/JSEN.2021.3136212.

[3] E. Vorathin, Z. M. Hafizi, A. M. Aizzuddin, M. K. A. Zaini, and K. S. Lim, "Temperature-independent chirped FBG pressure transducer with high sensitivity," *Opt. Lasers Eng.*, vol. 117, pp. 49–56, Jun. 2019, doi: 10.1016/j.optlaseng.2019.01.012.

[4] S. Zhu, M. Liu, H. Song, C. Li, X. Yang, and X. Chen, "An integrated dual-parameter sensor based on FBG for temperature/pressure monitoring of fluid pipeline," *Opt. Fiber Technol.*, vol. 84, May 2024, Art. no. 103694, doi: 10.1016/j.yofte.2024.103694.

[5] G. Hegde, M. V. N. Prasad, and S. Asokan, "Temperature compensated diaphragm based fiber Bragg grating (FBG) sensor for high pressure measurement for space applications," *Microelectron. Eng.*, vol. 248, Aug. 2021, Art. no. 111615, doi: 10.1016/j.mee.2021.111615.

[6] Z. Jia, Q. Fan, D. Feng, D. Yu, X. Zhao, and K. Yang, "Design and investigation of the fiber Bragg grating pressure sensor based on square diaphragm and truss-beam structure," *Opt. Eng.*, vol. 58, no. 9, p. 1, Sep. 2019, doi: 10.1117/1.oe.58.9.097109.

[7] L. Ji et al., "High-resolution fiber grating pressure sensor with in-situ calibration for deep sea exploration," *Opt. Exp.*, vol. 31, no. 6, pp. 10358–10367, Mar. 2023, doi: 10.1364/OE.484406.

[8] Z. Hong-kun, Z. Yong, Z. Qiang, and L. Ri-qing, "High sensitivity optical fiber pressure sensor based on thin-walled oval cylinder," *Sens. Actuators A, Phys.*, vol. 310, Aug. 2020, Art. no. 112042, doi: 10.1016/j.sna.2020.112042.

[9] W. Wu, B. Sun, S. Chen, W. Gong, and H. Wei, "Membrane-based optical fiber Bragg grating pressure sensor for health monitoring of pile foundations," *Appl. Opt.*, vol. 63, no. 12, p. 3039, 2024, doi: 10.1364/ao.514872.

[10] W. L. Yang, Y. L. Xiong, Q. Y. Li, X. M. Jin, and L. Wang, "Research on dual bellows FBG pressure sensor," *Appl. Mech. Mater.*, vols. 336–338, pp. 239–243, Jul. 2013, doi: 10.4028/www.scientific.net/amm.336-338.239.

[11] S. Xu, X. Li, T. Wang, X. Wang, and H. Liu, "Fiber Bragg grating pressure sensors: A review," *Opt. Eng.*, vol. 62, no. 1, 2023, Art. no. 010902, doi: 10.1117/1.Oe.62.1.010902.

[12] Z. Liu et al., "Design of a fiber Bragg grating pressure sensor based on a metal diaphragm and lever structure," *Sensors*, vol. 22, no. 14, p. 5096, Jul. 2022, doi: 10.3390/s22145096.

[13] D. Feng, D. Xu, F. Chen, Q. Chen, and X. Qiao, "An FBG temperature–pressure sensor based on diaphragm and special-shaped bracket structure," *IEEE Sensors J.*, vol. 23, no. 4, pp. 3589–3596, Feb. 2023, doi: 10.1109/JSEN.2022.3232142.

[14] X. Liu, L. Liang, K. Jiang, and G. Xu, "Sensitivity-enhanced fiber Bragg grating pressure sensor based on a diaphragm and Hinge-lever structure," *IEEE Sensors J.*, vol. 21, no. 7, pp. 9155–9164, Apr. 2021, doi: 10.1109/JSEN.2020.3045992.

[15] L. Zhang et al., "Design of fiber Bragg grating sensor for static ice pressure detection," *Opt. Fiber Technol.*, vol. 86, Sep. 2024, Art. no. 103845, doi: 10.1016/j.yofte.2024.103845.

[16] C. Li, X. Tong, W. Huang, Y. Wang, and F. Zeng, "Diaphragm FBG pressure sensor for high precision measurement in low pressure environments," *Opt. Fiber Technol.*, vol. 87, Oct. 2024, Art. no. 103917, doi: 10.1016/j.yofte.2024.103917.

[17] Q. Shu, L. Wu, S. Lu, and W. Xiao, "High-sensitivity structure based on fiber Bragg grating sensor and its application in nonintrusive detection of pipeline pressure change," *Measurement*, vol. 189, Feb. 2022, Art. no. 110444, doi: 10.1016/j.measurement.2021.110444.

[18] L. Qiang et al., "FBG demodulation method based on long-period fiber gratings," *J. Appl. Opt.*, vol. 43, no. 1, pp. 160–166, 2022, doi: 10.5768/jao202243.0108002.

[19] V. S. C. S. Vaddadi, S. R. Parne, V. P. Vijeesh, S. Gandi, S. S. S. Panda, and L. R. Cenkeramaddi, "Design and fabrication of liquid pressure sensor using FBG sensor through seesaw Hinge mechanism," *IEEE Photon. J.*, vol. 14, no. 5, pp. 1–7, Oct. 2022, doi: 10.1109/JPHOT.2022.3210146.

[20] L. Qiang et al., "Fiber Bragg grating temperature and pressure sensor based on Hinge lever structure," *Chin. Opt.*, vol. 18, no. 1, pp. 63–69, 2025, doi: 10.37188/co.2024-0090.

[21] G. Chen, J. Jia, X. Liu, and Y. Gou, "Design calculation and analysis of elliptical flexure Hinges," *Eng. Mech.*, vol. 23, no. 5, pp. 152–156, 2006.

[22] Y. Zhang, "Calculation of stress stiffness and effective area of diaphragm with hardpan," *J. Propul. Power*, vol. 18, pp. 65–68, Apr. 2006.

[23] J. Y. Shen, H. J. Zhang, and Y. Zhao, "Calculation method of magnification ratio for lever-type flexure Hinge mechanism driven by piezoactuator," *Trans. Chin. Soc. for Agricult. Machinery*, vol. 44, no. 9, pp. 267–271, Sep. 2013.

[24] J. Wang et al., "Ultra-high sensitivity photonic crystal fiber sensor based on dispersion turning point sensitization of surface plasmonic polariton modes for low RI liquid detection," *Opt. Exp.*, vol. 32, no. 19, p. 32895, 2024, doi: 10.1364/oe.531112.

[25] D. Xu, D. Feng, Q. Chen, G. Liu, and X. Qiao, "Small-sized temperature and pressure sensors based on fiber Bragg grating for oil and gas wells," *Sens. Actuators A, Phys.*, vol. 357, Aug. 2023, Art. no. 114397, doi: 10.1016/j.sna.2023.114397.

[26] V. S. C. S. Vaddadi, S. R. Parne, S. Afzulpurkar, S. Prabhu Desai, and V. Vadakke Parambil, "Design and development of pressure sensor based on fiber Bragg grating (FBG) for ocean applications," *Eur. Phys. J. Appl. Phys.*, vol. 90, no. 3, p. 30501, Jun. 2020, doi: 10.1051/epjap/2020200036.

[27] E. Vorathin, Z. M. Hafizi, A. M. Aizzuddin, and K. S. Lim, "Temperature-insensitive pressure transducer based on reflected broadened spectrum with enhanced sensitivity," *Sens. Actuators A, Phys.*, vol. 288, pp. 61–66, Apr. 2019, doi: 10.1016/j.sna.2019.01.028.

Qiang Liu received the bachelor's, master's, and Ph.D. degrees from Harbin Engineering University, Harbin, China, in 2003, 2006, and 2012, respectively.

He is currently a Professor with Northeast Petroleum University, Daqing, China. His research interests include optical fiber sensing technology and microstructured optical fiber design.

Dr. Liu is a Senior Member of the Chinese Optical Society.

Shuhui Wei received the bachelor's degree in communication engineering from Shandong University of Technology, Zibo, China, in 2023. He is currently pursuing the master's degree with Northeast Petroleum University, Daqing, China.

His research interests include optical fiber sensing technology.

Shenglong Gu, photograph and biography not available at the time of publication.

Jian Han, photograph and biography not available at the time of publication.

Chao Ma, photograph and biography not available at the time of publication.

Pengfei Lu, photograph and biography not available at the time of publication.

Jingwei Lv, photograph and biography not available at the time of publication.

Paul K. Chu (Fellow, IEEE), photograph and biography not available at the time of publication.

Chao Liu received the bachelor's degree from Heilongjiang University, Harbin, China, in 2002, and the master's and Ph.D. degrees from Harbin Institute of Technology, Harbin, in 2004 and 2008, respectively.

Currently, he is a Professor with Northeast Petroleum University, Daqing, China. His research interests include optical fiber sensing technology, surface plasmon resonance, and nanophotonics.